Two-photon fluorescence microscopy signal formation in highly scattering media: theoretical and numerical simulation

E.A. Sergeeva, A.R. Katichev, M.Yu. Kirillin

Abstract. **Using the radiative transfer theory and Monte Carlo simulations, we analyse the effect of scattering in a medium and of the size of the detector pinhole on the formation of the fluorescent signal in standard two-photon fluorescence microscopy (TPFM) systems. The theoretical analysis is based on a small-angle diffusion approximation of the radiative transfer equation, adapted to calculate the propagation of focused infrared radiation in media similar to the biological tissues in their optical properties. The accuracy of the model is evaluated by comparing the calculated excitation intensity in a highly scattering medium with the results of Monte Carlo simulations. To simulate a tightly focused Gaussian beam by the Monte Carlo method, the so called 'ray-optics' approach that correctly takes into account the finite size and shape of the beam waist is applied. It is shown that in the combined confocal and two-photon scanning microscopy systems not equipped with an external 'nondescanned' detector, the scattering significantly affects both the nonlinear excitation efficiency in the medium and the fluorescence collection efficiency of the system. In such systems, the rate of the useful TPFM signal in-depth decay is 1.5 – 2 times higher than in systems equipped with a 'nondescanned' detector.**

1. Introduction

Among the optical methods of biomedical diagnostics, which use near-IR radiation ($\lambda_{ex} = 700 – 1000$ nm), two-photon fluorescence microscopy (TPFM) is distinguished by a unique combination of submicron spatial resolution, high-contrast imaging and visualisation of the biotissue structure at depths of up to 1 mm [1]. The TPFM is mainly used to observe the signals of the collective or individual activity of neurons in the brain of laboratory animals *in vitro* and *in vivo* [2], as well as for three-dimensional visualisation of unstained integumentary tissues *in vivo* [3]. The theoretically predicted maximum observation depth of the TPFM method is limited by the multiple scattering effects [4, 5]; however, to achieve it in practice, maximisation of the fluorescence excitation and detection efficiency is required. The first problem can be

E.A. Sergeeva, A.R. Katichev, M.Yu. Kirillin Institute of Applied
Physics, Russian Academy of Sciences, ul. Ul'yanova 46,
603950 Nizhnii Novgorod, Russia; e-mail: sea@ufp.appl.sci-nnov.ru

solved by using fluorophores with the maximum in the two-photon excitation near $\lambda_{ex} = 1000$ nm[*], that are characterised by a large absorption cross section and photobleaching resistance. At present, quantum dots meet these requirements [6], but their use in *in vivo* experiments requires a further study of their accumulation, excretion, and toxicity. More acceptable from the standpoint of security and functionality are coloured proteins that fluoresce in the visible range when excited in the region from 850 to 1000 nm [2], but their two-photon absorption cross section is two orders of magnitude lower than that of quantum dots. In this way, efficient detection of a fluorescence signal is an urgent problem that also involves optimisation of the collection efficiency of the imaging system.

Laser scanning microscopy (LSM) systems equipped with the so-called nondescanned detector measuring the fluorescence signal as close to the objective exit as possible [7] have the highest collection efficiency. At the same time, some LSM setups (in particular, the systems combining confocal and two-photon fluorescence microscopy) are equipped with a universal confocal detector with a pinhole whose size is adjustable in a wide range [8]. As in the case of confocal imaging, the two-photon excited fluorescence (TPEF) signal in such systems is 'descanned' (i.e., passes back through the same scanning optical elements as the probe beam), but its registration requires maximal opening of the detector pinhole. In visualising transparent objects, the presence of a confocal pinhole does not affect the collection efficiency of the combined LSM system; however, scattering reduces the TPEF detection efficiency [9]. It is known that this leads to a decrease in the working depths of the systems operating in the multiphoton regime; nevertheless, the quantitative estimates of this effect are absent in the literature.

Reducing the collection efficiency in scattering media with depth was studied mainly experimentally [7, 9, 10] or with the help of the numerical Monte Carlo (MC) simulation [10 – 12]. This effect was theoretically evaluated in [12] within the diffusion approximation of the radiative transfer theory. However, in biological tissues the small-angle rather than the diffuse scattering dominates in the range of working depths of the TPFM method. In this paper, we propose an improved analytical model to describe the TPEF signal measured from the scattering medium by two types of receivers: a nondescanned (NDS) receiver and a descanned receiver with an adjustable confocal pinhole (DSCP). The proposed model is based on the calculation of the light field in a scattering medium in the

---

[*] Despite the higher rate of water absorption, the penetration depth of radiation in the biological tissue at this wavelength is higher than that of radiation in range from 700 to 800 nm.

small-angle diffusion approximation for the radiative transfer equation. The validity of the developed model is confirmed by Monte Carlo simulations of the fluorescence signal, adapted to the transverse profile of the probe beam intensity and the type of receiver (NDS or DSCP). The completed study made it possible to compare quantitatively the characteristics of the signals detected by the TPFM imaging systems with different types of receivers.

2. Analysis of two-photon excitation of the fluorophore in a scattering medium

2.1. Models of an excitation beam

According to [8, 13], the number of fluorescence photons Q, generated in the volume V per unit time (photon s^{-1}) due to two-photon excitation of the fluorophore by a train of short pulses with a duration t and a repetition rate F, is defined by

$$Q = \int_V q(\boldsymbol{r}) \mathrm{d}\boldsymbol{r}, \quad q(\boldsymbol{r}) = \frac{\alpha \Sigma_2^* P_{\mathrm{ex}}^2}{2\tau F} C(\boldsymbol{r}) I_{\mathrm{ex}}^2(\boldsymbol{r}), \tag{1}$$

where $q(\boldsymbol{r})$ is the spatial density of the two-photon fluorescence sources; α is the form factor of the pulse; Σ_2^* is a dynamic two-photon absorption cross section (cm^4 s photon^{-1}); P_{ex} is the average excitation power (photon s^{-1}) at a wavelength λ_{ex}; $C(\boldsymbol{r})$ is the local concentration of the fluorophore; $I_{\mathrm{ex}}(\boldsymbol{r})$ is the intensity distribution (normalised to P_{ex}) in the studied volume [5, 13]. Two-photon fluorescence generation requires a high local instantaneous intensity (of the order of 10^{30} photon s^{-1} cm^{-2}), and so the excitation beam is usually sharply focused by an objective with a numerical aperture NA > 0.6. In a transparent medium, the intensity in the focused unit-power beam can be described by a Gaussian distribution:

$$I_{\mathrm{ex}}(\boldsymbol{r}) = \exp\left(-\frac{\boldsymbol{r}_\perp^2}{a^2(z)}\right)(\pi a^2(z))^{-1}, \tag{2}$$

where

$$a^2(z) = \left(0.61\frac{\lambda_{\mathrm{ex}}}{\mathrm{NA}}\right)^2 + \frac{(z - z_{\mathrm{f}})^2 \mathrm{NA}^2}{1.5\pi^2 n^2}$$

is the beam cross section at different depths z in a medium with the refractive index n; z_{f} is the depth of the beam waist location. The intensity distribution at any depth meets the normalisation condition

$$\int_\infty I_{\mathrm{ex}}(\boldsymbol{r}_\perp, z)\mathrm{d}^2\boldsymbol{r}_\perp = 1.$$

When a focused Gaussian beam propagates in the tissue, its structure is distorted due to scattering (we neglect the linear absorption of IR radiation in the range of TPFM working depths). The total intensity in the excitation unit-power beam in a medium with the scattering coefficient μ_{ex} is the sum of unscattered or ballistic (I_{b}) and scattered (I_{s}) components [14]:

$$I_{\mathrm{ex}}(\boldsymbol{r}_\perp, z) = I_{\mathrm{b}}(\boldsymbol{r}_\perp, z) + I_{\mathrm{s}}(\boldsymbol{r}_\perp, z), \tag{3}$$

where

$$I_{\mathrm{b}}(\boldsymbol{r}_\perp, z) = \exp\left(-\frac{\boldsymbol{r}_\perp^2}{a^2(z)} - \mu_{\mathrm{ex}}z\right)(\pi a^2(z))^{-1}.$$

The component I_{s} can be found by solving the radiative transfer equation taking into account the pronounced scattering anisotropy in biological tissues (the mean cosine of the single-scattering angle $g > 0.8$). In our previous paper [5] we considered the solution for the I_{s} in the form of a Gaussian distribution [15]:

$$I_{\mathrm{s}}(\boldsymbol{r}_\perp, z) = P_{\mathrm{s}}(z)\exp\left(-\frac{\boldsymbol{r}_\perp^2}{a_{\mathrm{s}}^2(z)}\right)(\pi a_{\mathrm{s}}^2(z))^{-1}. \tag{4}$$

The power P_{s} of the scattered intensity component and its cross section correspond to the integral characteristics of the beam of an arbitrary shape, calculated in the small-angle diffusion approximation [15]:

$$P_{\mathrm{s}}(z) = 1 - \exp(-\mu_{\mathrm{ex}}z),$$

$$a_{\mathrm{s}}^2(z) = a^2(z) + \frac{1}{3}\frac{\mu_{\mathrm{ex}}\langle\gamma^2\rangle z^3}{P_{\mathrm{s}}(z)}. \tag{5}$$

Here, $\langle\gamma^2\rangle$ is the dispersion of the small-angle scattering phase function. However, this solution ignores the fact that the source power for the diffuse intensity component, which is determined by the ballistic component of the focused beam, depends on the depth: near the focus the number of the scattered photons should increase because the density of unscattered photons is maximal there. In this paper, we compare the calculation results of the I_{s} structure, obtained using a standard small-angle diffusion approximation, with its modification proposed in [16], where the source of the scattered photons is distributed in depth. In the modified small-angle diffusion approximation, the expression for I_{s} has the form:

$$I_{\mathrm{s}}^*(\boldsymbol{r}_\perp, z) = \int_0^z \mu_{\mathrm{ex}}\exp\left(-\frac{\boldsymbol{r}_\perp^2}{S_{\mathrm{s}}^*(z, z_1)} - \mu_{\mathrm{ex}}z_1\right)(\pi S_{\mathrm{s}}^*(z, z_1))^{-1}\mathrm{d}z_1,$$

$$\tag{6}$$

$$S_{\mathrm{s}}^*(z, z_1) = a^2(z_1) + \frac{1}{3}\mu_{\mathrm{ex}}\langle\gamma^2\rangle(z - z_1)^3.$$

2.2. Model of a phase function

For further calculations, it is necessary to specify the model phase function, which would reflect the characteristics of single scattering in biological tissues. Traditionally, biotissue optics utilises the Henyey–Greenstein phase function [17]

$$p_{\mathrm{HG}}(\gamma, g) = \frac{1 - g^2}{[1 + g^2 - 2g\cos\gamma]^{3/2}}, \tag{7}$$

satisfying the normalisation condition

$$\frac{1}{2}\int_0^\pi p_{\mathrm{HG}}(\gamma, g)\sin\gamma\,\mathrm{d}\gamma = 1.$$

This function is convenient because the single parameter – the mean cosine of the scattering angle g – is used to specify it in the whole range of scattering angles γ. Indeed, the Henyey–Greenstein function well approximates many real phase functions in the region of small angles, but the corresponding parameter g turns out to be much larger than the anisotropy factor calculated from the measured phase function, and function (7) underestimates the integral value of the probability of scattering in the backward hemisphere. As alternative models, Sharma and Banerjee [18] proposed multicomponent phase functions; however, the number of independent parameters determining the partial contribution of the components and their shape increases. In this paper, we analyse a two-term phase function, consisting of small-angle and isotropic parts [5, 15]:

$$p(\gamma) = bp_1(\gamma) + (1 - b),\qquad(8)$$

where as the $p_1(\gamma)$ component we use a 'narrow' Henyey–Greenstein function $p_{HG}(\gamma, g')$, corresponding to the anisotropy factor $g' = (g + 1)/2$ [19]. The parameter $b = 2g/(1 + g)$ is determined from the equality of the anisotropy factors for the measured phase function and approximation (8). This model describes well the real phase functions of biotissues (Fig. 1) and also allows one to separate the contributions of scattering by small and large angles. For biotissues with $g > 0.7$, the scattering angle dispersion of the small-angle function p_1 is related to the anisotropy factor of the total phase function by the phenomenological expression:
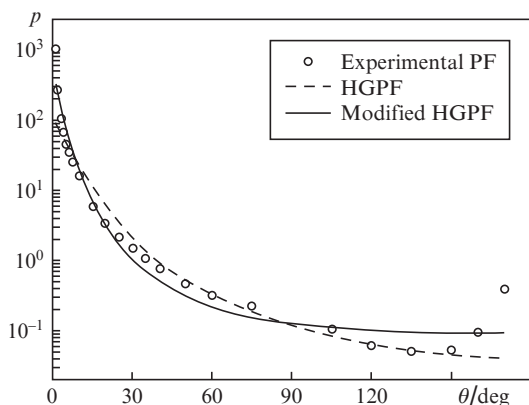
$$\langle \gamma^2 \rangle \cong 0.72(1 - g).\qquad(9)$$

Figure 1. Scattering phase function (PF) of the rat brain sample [20], characterised by the anisotropy factor $g = 0.88$ and its approximation by the standard Henyey–Greenstein phase function (HGPF) and modified HGPF (8) for the same value of g.

We subsequently used the modified Henyey–Greenstein phase function to simulate the propagation of the focused beam in a scattering medium by the Monte Carlo method and to compare the results of simulation and theory.

2.3. Monte Carlo simulation of propagation of a tightly focused excitation beam in a scattering medium

To test the analytical models of the excitation beam scattering we compared the beam profiles, calculated by formulas of standard [(3)–(5)] and modified [(3), (6)] small-angle diffusion

approximations, with the results of the Monte Carlo simulation. The latter method is widely used in problems of biomedical optics, acting as a 'numerical experiment,' but is mainly employed for studying the propagation of radiation from collimated sources. Simulation of tightly focused beams is significantly simplified: the beam waist is usually considered to be a point [21, 22]. However, in calculating the signals recorded by different optical microscopy systems, the finiteness of the radius of the focused beam waist is an important factor determining, in particular, the longitudinal and transverse resolution of the method. At the same time, the classical implementation of the Monte Carlo simulation of light propagation in transparent and scattering media [23] suggests that the photons do not have the wave properties and propagate along straight paths in free space (or between scattering events). This makes the description of the diffraction pattern of a Gaussian beam extremely difficult.

In this paper, we simulated the beam focused by an objective with a numerical aperture NA ≥ 0.6 with the help of the 'ray-optics' approach [24], which in a transparent medium ensures the correspondence of the beam profile to expression (2) at any depth. In accordance with this approach, the initial position of the photon (x_0, y_0) in the plane of the output pinhole of the objective ($z_0 = 0$) is determined by the Box–Muller transform:

$$x_0 = \frac{a(z_0)}{\sqrt{2}} \cos(2\pi\varepsilon_1)\sqrt{-2\ln\varepsilon_2},$$

$$y_0 = \frac{a(z_0)}{\sqrt{2}} \sin(2\pi\varepsilon_1)\sqrt{-2\ln\varepsilon_2},$$

where ε_1 and ε_2 are the independent random variables uniformly distributed on the interval (0,1). This transformation provides a Gaussian intensity distribution in the plane of the output pinhole of the objective with a width $a(0) \cong z_f\text{NA}/(\pi n)$. The initial direction of photons is determined by the vector connecting a point in the plane $z_0 = 0$ and a point in the focal plane of the objective (z_f), defined by the same transform:

$$x_f = \frac{a_0}{\sqrt{2}} \cos(2\pi\varepsilon_3)\sqrt{-2\ln\varepsilon_4},$$

$$y_f = \frac{a_0}{\sqrt{2}} \sin(2\pi\varepsilon_3)\sqrt{-2\ln\varepsilon_4},$$

where ε_3 and ε_4 are the independent random variables uniformly distributed on the interval (0,1); $a_0 = 0.61\lambda_{ex}/\text{NA}$ is the waist radius.

The ray-optics approach to simulation of the tightly focused Gaussian beam allows one to accurately reproduce the intensity profile (calculated by the analytical formula) in a nonscattering medium (Fig. 2). The main parameters of the Gaussian beam – the position of the waist, its longitudinal and transverse dimensions – correspond to analytical quantities. This allows one to effectively use this approach for simulating the propagation of the focused beam in a scattering medium.

Figures 3 and 4 show the axial and transverse profiles of the focused excitation beam in a scattering medium, calculated using Monte Carlo simulation and the formulas of standard
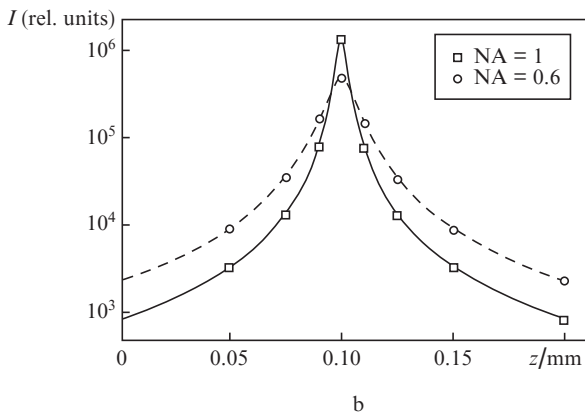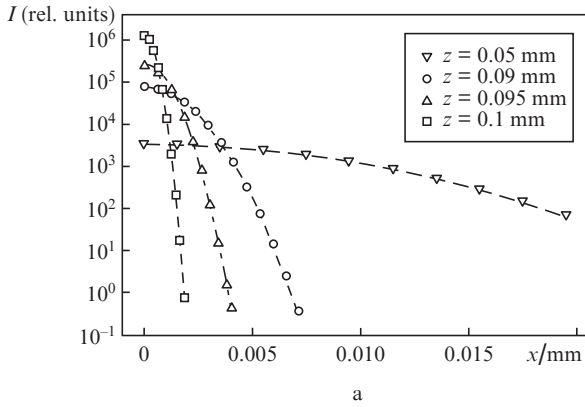
Figure 2. Transverse intensity profiles at different depths z (a) and longitudinal axial intensity profiles of the Gaussian beam focused to a depth $z_f = 0.1$ mm in a nonscattering medium at $\lambda_{ex} = 800$ nm for different numerical apertures NA of the objective (b). Curves are calculations by formula (2), points are the result of Monte Carlo simulations using the ray-optics approach.

and modified small-angle diffusion approximations (indicated in the figures as the SSADA and MSADA, respectively). 250 million photons were used in simulations. After generating the initial position and direction of the photon propagation in accordance with the above procedure, further propagation of the photons in a scattering medium was simulated using standard algorithms [21, 23]. The change in the direction of a photon in each scattering event was determined in accordance with the phase function (8). One can see from the plots that for the depths from the medium surface to the focal beam waist, the modified theory better agrees with the simulation results than the standard small-angle diffusion approximation; however, behind the focus, the both models demonstrate the discrepancy with the numerical results. Nevertheless, the modified theory has an advantage consisting in the fact that it more accurately describes the transverse intensity profile, whereas the SSADA model gives underestimated intensities near the beam axis (Figs 4a,c). At the same time, at depths exceeding 1 mm, the analytically calculated intensity for standard and modified small-angle diffusion approximations is significantly lower than the intensity calculated using Monte Carlo simulations (Fig. 3c). This is explained by the fact that at depths of more than one transport length $l_t = [\mu_{ex}(1 - g)]^{-1}$, the evolution of the beam shape is determined not by small-angle but by diffuse scattering, which is neglected both in SSADA and MSADA. For the chosen parameters of the medium, the transport length is 1 mm. Note also that in the
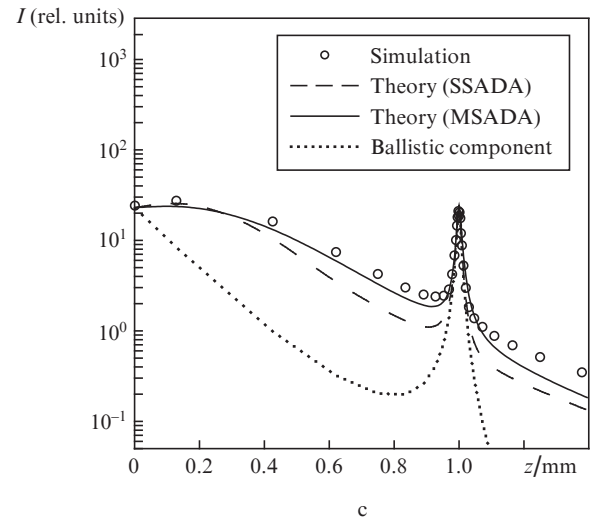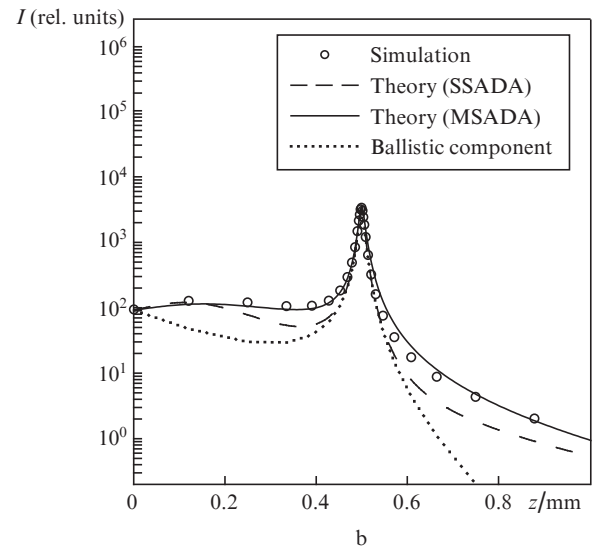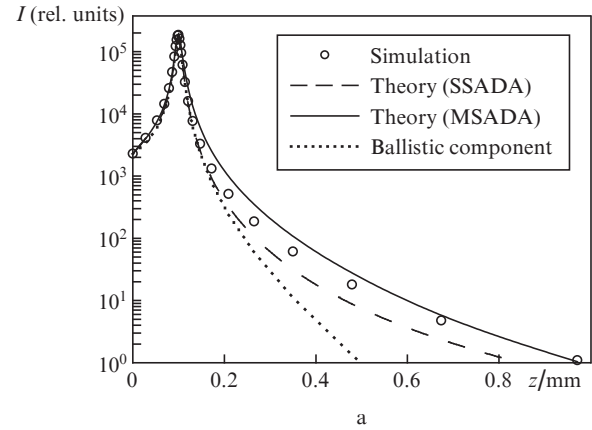

Figure 3. Axial intensity profiles in a Gaussian beam focused in a scattering nonabsorbing medium with the refractive index $n = 1.33$, the scattering coefficient $\mu_{ex} = 10$ mm^{-1}, and the anisotropy factor $g = 0.9$ at NA = 1, $\lambda_{ex} = 800$ nm, and $z_f = 100$ (a), 500 (b), and 1000 μm (c).

whole range of the depths examined, the intensity in the beam focus is determined mainly by ballistic photons (see Fig. 3). However, when the focusing depth is close to one transport length, the total intensity near the medium surface becomes comparable with the intensity in the waist (Fig. 3c), which
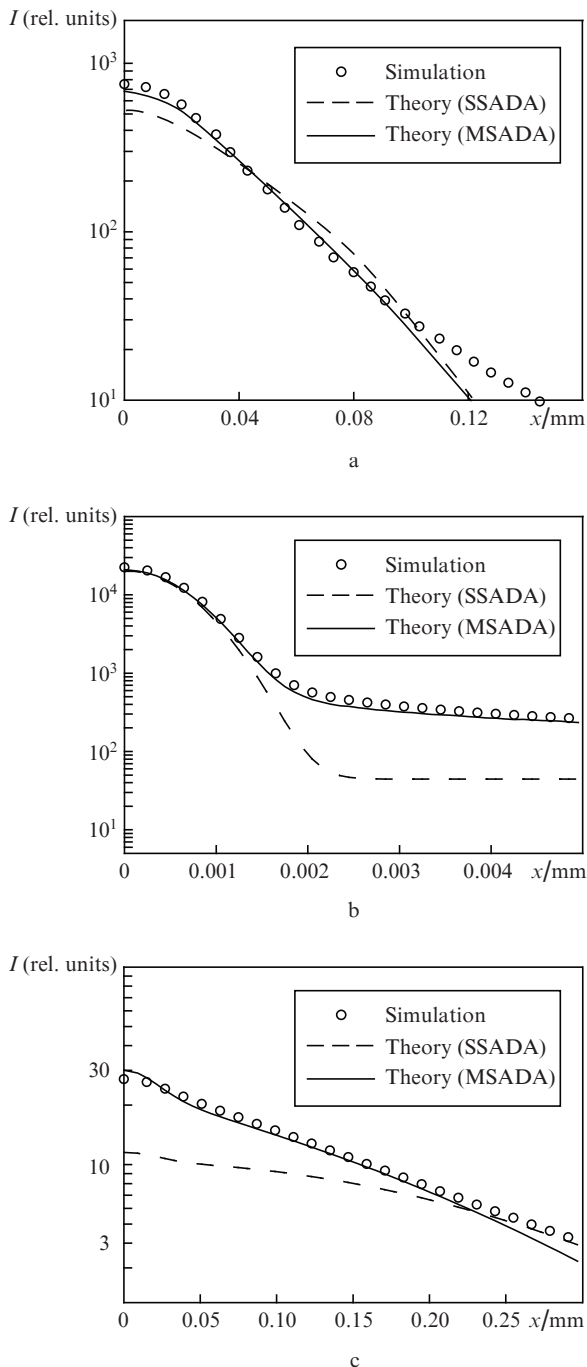
Figure 4. Transverse intensity profiles in a Gaussian beam (NA = 1, λ_{ex} = 800 nm) focused at a depth z_f = 500 μm in a scattering nonabsorbing medium with n = 1.33, μ_{ex} = 10 mm^{-1}, and g = 0.9. The profiles are calculated in the planes z = 250 (a), 500 (b), and 750 μm (c).

hinders the observation of deep-seated layers. In general, we can conclude that in the medium regions involved significantly in the formation of the TPEF signal, the MSADA model better agrees with the results of the Monte Carlo simulation and is, therefore, more preferable for further use.

2.4. TPEF signal distribution in a bulk fluorescent medium

Using the beam model developed, we can analyse which regions of the strongly scattering and fluorescence medium make the main contribution to the TPEF signal, if the fluoro-phore is uniformly distributed in the medium. This corresponds to the problem of observation of thick tissue samples when fluorophore accumulates in the tissue volume. The TPEF power $Q = Q(z_f)$ is a function of the observation depth, determined by the position of the excitation beam focus in the medium. The authors of [4, 5, 25] showed that in a bulk fluorescent medium, interference of the near-surface fluorescence signal with a useful signal becomes significant. To study this effect, we consider the axial TPEF power distribution $W(z, z_f)$, which can be calculated by integrating the density of the fluorescence sources $q(\mathbf{r})$ along the transverse coordinate:

$$W(z, z_f) = \int_S q(\mathbf{r}) \mathrm{d}^2 \mathbf{r}_\perp = \frac{\alpha \Sigma_2^* P_{ex}^2}{2\tau F} C_0 \int_S I_{ex}^2(\mathbf{r}_\perp, z, z_f) \mathrm{d}^2 \mathbf{r}_\perp. \quad (10)$$

To analyse quantitatively Q and W, the intensity $I_{ex}(\mathbf{r}_\perp, z, z_f)$ in the excitation beam will be calculated by MSADA formulas (3), (6). Figure 5 shows the TPEF power $Q(z_f)$ on the focusing depth in the scattering medium, and Fig. 6 shows the profiles of the axial distribution of the fluorescence power $W(z, z_f)$, corresponding to the various positions of the beam focus. If we assume that the fluorescence in the medium occurs only due to the nonlinear excitation of the fluorophore in the vicinity of the focus by unscattered light, then according to the Lambert–Beer law, the function $Q(z_f)$ should decrease with depth as $\exp(-2\mu_{ex}z_f)$, which corresponds to a square-law decay of the intensity I_b in the focus. However, the behaviour of the curve in Fig. 5 differs from the described law: the decay near the surface is close to exponential but is characterised by a somewhat lower rate, and at some depth the rate of the signal decay slows down. Comparing the curves in Figs 5 and 6, we can see that the first difference is due to the influence of scattered light on the intensity in the focus, and the second difference is due to the emergence of a high-power TPEF signal near the boundary, which is first comparable with the signal from the focus region, and then begins to exceed it. The local near-surface TPEF powers are small, but the region that produces this signal is considerably larger than the region of the focal volume. The influence of the near-surface illumination can be reduced by limiting the detector pin-hole, as envisaged in the DSCP schemes; however, when such a pinhole is absent (for example, in systems equipped with the NDS-detector), the visualisation depth by the high-contrast TPFM method is limited (Fig. 7).
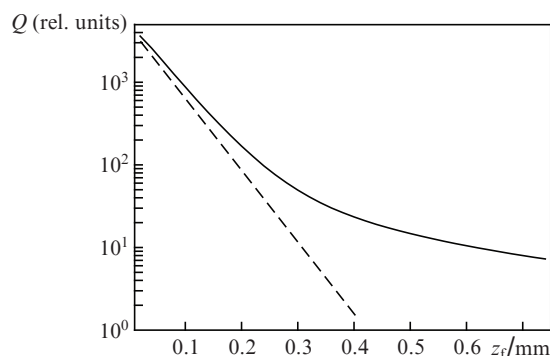

Figure 5. TPEF power as a function of the excitation beam focusing depth (NA = 1, λ_{ex} = 800 nm) in a scattering medium with n = 1.33, μ_{ex} = 10 mm^{-1}, g = 0.9 (solid curve); the dashed curve is the exponential asymptote $\exp(-2\mu_{ex}z_f)$.
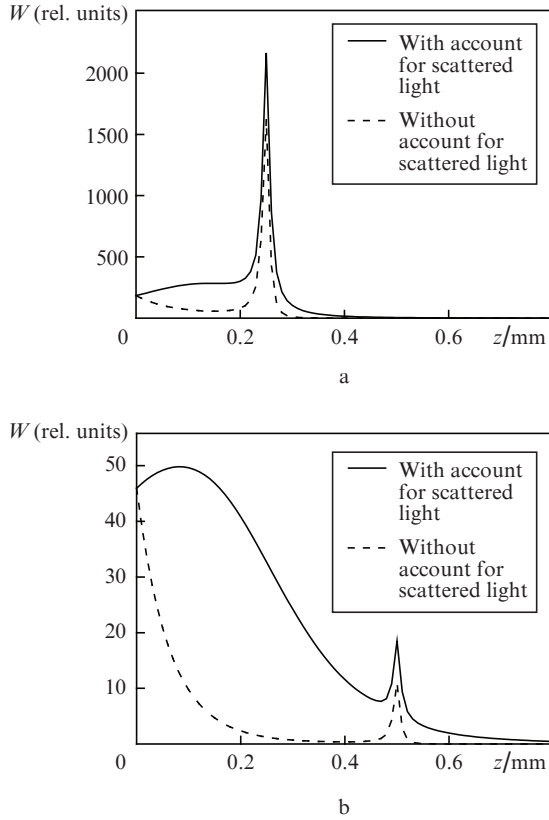
Figure 6. Axial distribution function of the TPEF power W for different excitation beam focusing depths (NA = 1, λ_{ex} = 800 nm) in a scattering medium with n = 1.33, μ_{ex} = 10 mm^{-1}, g = 0.9 at z_f = 250 (a) and 500 μm (b).
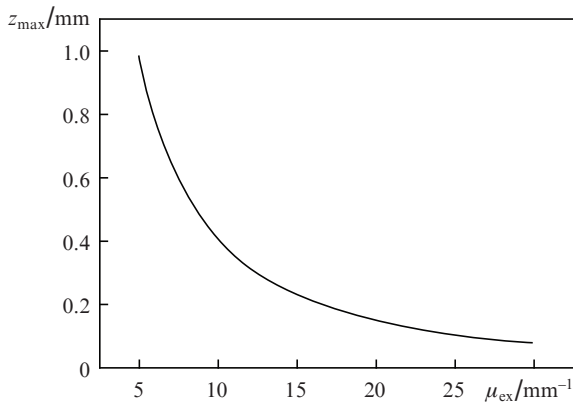

Figure 7. Maximum depth z_{max} (limited by the near-surface illumination) of visualisation of the scattering and bulk fluorescent medium structure by the TPFM method at NA = 1, λ_{ex} = 800 nm, g = 0.9, and n = 1.33.

3. Evaluation of the fluorescence collection efficiency of laser scanning microscopy setups equipped with nondescanned and descanned detector in a scattering medium

3.1. Analytic and numerical calculations of the fluorescence collection efficiency of TPFM systems

The TPFM image is characterised by the fluorescence power, which is measured from the medium at a given position of the focus $r_f = (r_{f\perp}, z_f)$ [15]:

$$P_{2PM}(r_f) = \int A(r_\perp, s) \mathrm{d}^2 r_\perp \mathrm{d}s \int q(r', r_f) L_0(r_\perp - r', s) s_z \mathrm{d}r'. \quad (11)$$

Here, the function $L_0(r_\perp - r', s)$ describes the spatial-angular distribution of fluorescence in the plane of the medium boundary at point $r_\perp$ and in the direction s from the unit-power isotropic source located in the medium at point r'; $A(r_\perp, s)$ is the spatial-angular characteristic of the receiver. Formula (11) takes into account that the receiver pinhole illuminated by fluorescence is oriented parallel to the medium boundary and has an outer normal in the direction of the z axis. For a point fluorophore positioned in the focus, $q(r', r_f) = Q\delta(r' - r_f)$, and formula (11) takes the form:

$$P_{2PM}(r_f) = Q \int A(r_\perp, s) L_0(r_\perp - r_f, s) s_z \mathrm{d}^2 r_\perp \mathrm{d}s. \quad (12)$$

The integrand in (12) is the collection efficiency of the TPFM imaging system, which is the ratio of the number of fluorescence photons reaching the photodetector to the number of photons produced in a fluorescent medium due to two-photon absorption:

$$\eta(r_f) = \int A(r_\perp, s) L_0(r_\perp - r_f, s) s_z \mathrm{d}^2 r_\perp \mathrm{d}s. \quad (13)$$

Under the scattering conditions, the collection efficiency depends not only on the characteristics of the receiver but also on the optical parameters of the medium at the fluorescence wavelength.

We will use the scattering model developed in the previous section to assess quantitatively the collection efficiency of two types of recording systems: a wide receiving pinhole (corresponding to a TPFM system equipped with a NDS-receiver) and a limited receiving pinhole (corresponding to a TPFM system with a DSCP-receiver). We assume that generation of the fluorescence photons due to two-photon absorption occurs mainly in the region of the focal volume, which does not exceed a few cubic micrometres in the case of tight focusing, and to simplify the resultant formulas, the fluorescence source can be treated as a point source. In a scattering medium, this assumption is valid for depths corresponding to the working range of the TPFM method, i.e. when the fluorescence from the beam waist is much higher than the volume fluorescence signal from the near-surface region. For a medium with a known scattering coefficient μ_{ex}, the maximum focusing depth satisfying this condition can be determined from the dependence in Fig. 7. For greater depths, the collection efficiency should be calculated using expression (11) with allowance for the nonlocal distribution of the TPFM sources.

In the standard small-angle diffusion approximation, the function L_0 in the medium at a distance r from a point isotropic source is given by [26]

$$L_0(r, \varphi) = \frac{1}{4\pi r^2}\left[\exp(-\mu_{em} r)\frac{\delta(\varphi)}{2\pi\sin\varphi}\right.$$

$$\left. + \frac{1 - \exp(-\mu_{em} r)}{\pi D}\exp\left(-\frac{\varphi^2}{D}\right)\right], \quad (14)$$

where φ is the angle of the vector deviation s from the radial direction; μ_{em} is the scattering coefficient at the wavelength of fluorescence emission λ_{em}; $D = \mu_{em}\langle\gamma^2\rangle r/3$ is the angular dis-

persion of the scattered radiance component. We will characterise the system measuring the optical signal by two parameters: the opening angle θ_{NA} of the numerical aperture of the objective (in TPFM systems, fluorescence is excited and measured by the same objective) and the quantity a_c, which is the effective field of view radius in the focal plane of the objective (Fig. 8). The value of a_c is related to a physical radius of the detector pinhole R through the parameters of the optical magnification of the objective (M_o) and microscope (M_m): $a_c = R/(M_o M_m)$ [27]. In addition to the above parameters, the collection efficiency of a real system depends on the transmission characteristics of the objective and other optical elements, but this dependence can be easily taken into account by multiplying by appropriate coefficients. In turn, the dependence of η on a_c will be more complicated because the quantity a_c limits the region of the angular sensitivity in the confocal detection scheme [11]. Formally, the influence of the confocal pinhole can be described by the presence of the angular filter of the fluorescence photons with the transmission characteristic

$$T \cong \exp\left(-\frac{\varphi^2 r^2}{a_c^2 \cos^2\theta}\right),$$

where θ is the angle between the symmetry axis and the direction to a point of photon emission from a scattering medium (Fig. 8). The nondescanned detector contains no limiting pinhole and allows one to take all the photons that fall within the numerical aperture of the objective. Therefore, in the case of NDS-receiver, the quantity a_c is chosen infinitely large. By this means the restriction on the direction of the arrival of photons involved in the formation of the fluorescence signal from a scattering medium is removed.
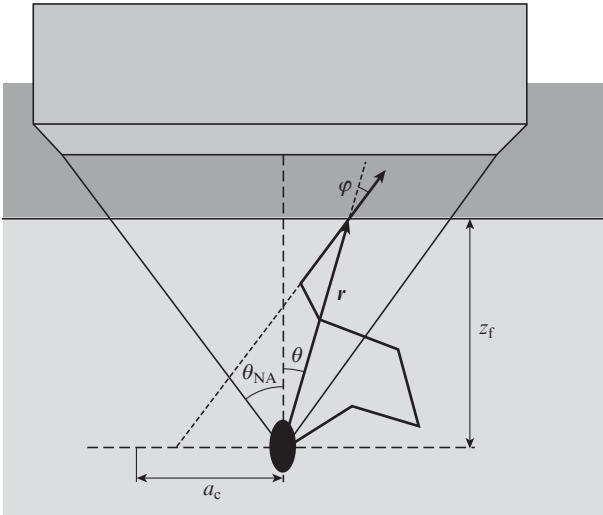

Figure 8. Scheme of the fluorescence signal detection in setups with a limited field of view [12].

The objective pinhole spatially restricts the area, from which the fluorescence flow is recorded, by a circle with an outer radius $r_\perp^* = z_f \cos\theta_{NA}$. Thus, the spatial-angular characteristic of the receiver A can be represented in the form:

$$A(r_\perp, \theta, \varphi) = \exp\left(-\frac{\varphi^2 r_\perp^2}{a_c^2 \cos^2\theta \sin^2\theta}\right)\Phi(z_f \cos\theta_{NA} - r_\perp), \quad (15)$$

where $\Phi(\cdot)$ is the Heaviside function, and the collection efficiency is expressed by the formula

$$\eta(z_f) = \frac{1}{2}\int_{\cos\theta_{NA}}^1 \left[\exp(-\mu_{em}z_f/x) + (1 - \exp(-\mu_{em}z_f/x))\right.$$

$$\left.\times \frac{a_c^2 x^2}{\mu_{em}\langle\gamma^2\rangle z_f^3/3x^3 + a_c^2 x^2}\right]dx. \quad (16)$$

This expression is based on the calculation of radiance using a standard small-angle diffusion approximation. However, the above comparison of the small-angle diffusion approximation with Monte Carlo simulations showed that the theory gives underestimated values of the local intensity near the symmetry axis of the system. In this case, it will lead to an underestimation of the collection efficiency of the imaging system. Therefore, we have refined expression (15) by analogy with formula (6), taking into account the distribution of the source of scattered photons in the case of a standard small-angle diffusion approximation:

$$\eta^*(z_f) = \frac{1}{2}\int_{\cos\theta_{NA}}^1 \left[\exp(-\mu_{em}z_f/x) + a_c^2 x^2\right.$$

$$\left.\times \int_0^{z_f/x} \frac{\mu_{em}\exp(-\mu_{em}z_1)}{\mu_{em}\langle\gamma^2\rangle(z_f/x - z_1)^3/3 + a_c^2 x^2}dz_1\right]dx. \quad (17)$$

For a nonscattering medium from (16) and (17), we can obtain an obvious result: $\eta_0 = (1 - \cos\theta_{NA})/2$. For scattering media, Fig. 9 presents the calculation results of the collection efficiency of the systems equipped with NDS- and DSCP-receivers, and data of MC simulations. The numerical simulation was based on the calculation of the transport of photons (generated by a point isotropic source in the excitation beam focus) to the boundary of a scattering medium with the scattering coefficient μ_{em} and the scattering phase function (8), and on the spatial-angular filtration of outgoing photons in accordance with condition (15). For convenience of calculations, the value of a_c is given in units of the Airy disk radius (AU) for a given λ_{em} and numerical aperture of the objective. The receiver pinhole, which opens one Airy disk in the focal plane of the objective (1 AU = $0.61\lambda_{em}$/NA), provides ideal confocal detection of the fluorescence signal; for a system with a NDS-receiver, $a_c \to \infty$ (indicated as "NDS" in the figure).

Comparing the results of analytical calculations of the collection efficiency with the data of Monte Carlo simulations confirms the validity of model (17) in the studied range of localisation depths of a small fluorescent object. In general, the given dependences show that limiting the detection region by the confocal pinhole substantially affects the η^*. The collection efficiency of an ideal confocal pinhole ($a_c = 1$ AU) decreases exponentially with depth; however, an increase in the pinhole size by 10 and even 25 times did not significantly alter the rate of $\eta^*(z_f)$, which decreases only at pinholes with $a_c > 100$ AU. In this case, even for a pinhole of this size the collection efficiency turns to be significantly lower than η_0, if the fluorophore is located at a depth of more than a few scattering lengths, $l_{em} = 1/\mu_{em}$.

Quantitative assessment of the effect of scattering on the collection efficiency of the TPFM system is performed for the Carl Zeiss LSM 510 setup. The maximum physical size of the receiving pinhole in such a setup ($2R = 1000$ μm) corre-
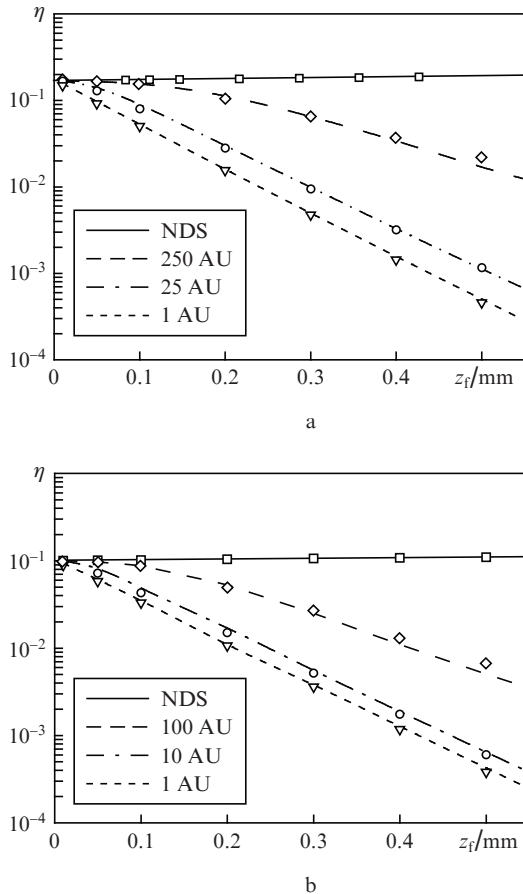
Figure 9. Collection efficiency of the TPFM system in a scattering medium ($\mu_{em} = 10$ mm^{-1}, $g = 0.9$, $n = 1.33$) as a function of the focusing depth for different values of a_c, measured in units of the Airy disk radius (AU) at $\lambda_{em} = 500$ nm, NA = 1 (a) and 0.8 (b). Lines correspond to theoretical calculations; points, to Monte Carlo simulations for the same values of a_c.

sponds to the field of view with a diameter $2a_c = (300/M_o)$ μm in the focal plane of the objective. For a standard water-immersion objective 20$^\times$/1.0 ($M_o = 20$, NA = 1), the transverse size of the detection system sensitivity is 15 μm, which corresponds to $a_c = 25$ AU for $\lambda_{em} = 500$ nm. With such a field of view, the collection efficiency of the TPFM system from depths, exceeding one scattering length, is close to that of the confocal detection scheme and decreases with depth approximately according to the law $\exp(-\mu_{em} z_f)$ (Fig. 9a).

3.2. Effect of the fluorescence collection efficiency on the TPFM signal

A decrease in the collection efficiency with increasing the focusing depth in the scattering medium will affect the rate of the TPFM signal decay. The brightness of each pixel of the TPFM image is determined by the number of fluorescence photons $N(z_f)$, arriving at the receiver during the dwell-time Δt of signal accumulation:

$$N(z_f) = P_{2PM}(z_f)\,\Delta t \cong Q(z_f)\,\eta(z_f)\,\Delta t.$$

This relation is applicable in a situation when two-photon excitation of the fluorophore is concentrated in the vicinity of the focus, and the effects of surface illumination can be

neglected. Figure 10 demonstrates the dependence of the TPFM signal, measured in a scattering medium by systems equipped with a NDS- or DSCP-receiver, on the focusing depth. It is obvious that the rate of the signal decay in systems with a NDS-receiver is much lower than in systems with a receiving pinhole whose size coincides with the diameter of the Airy disk (ideally confocal detection). However, increasing the size of the confocal receiving pinhole to 10–20 AU has virtually no effect on the change in the rate of TPFM signal decay. Thus, in the LSM systems equipped with a DSCP-receiver, the change in the detector pinhole size within acceptable limits does not lead, in practice, to a significant increase in the TPFM signal level achieved in systems with a NDS-detector. In the first approximation, the dependence of the TPFM signal on the depth can be evaluated for systems with a NDS-receiver as $N_{NDS}(z_f) \sim \exp(-2\mu_{ex}z_f)$. With allowance for the above, the TPFM signal in systems with an adjustable confocal pinhole decreases as $N_{DSCP}(z_f) \sim \exp[-(2\mu_{ex} - \mu_{em})z_f]$. For most biological tissues, the scattering coefficient μ_s is either independent of the wavelength in the range from 500 to 1000 nm [20] or decreases in accordance with the law that is close to the power law: $\mu_s \sim \lambda^{-m}$, where $m = 0.5–2$ [28]. For excitation in the near-IR region and fluorescence detection in the visible region, the scattering coefficients are related approximately as $\mu_{em}/\mu_{ex} \sim 1–2$. This implies that the total attenuation of the TPFM signal recorded by a receiver with a limited pinhole is $2\mu_{ex} + \mu_{em} = (3–4)\mu_{ex}$ and is 1.5–2 times higher than the attenuation of the TPFM signal recorder by the NDS-detector.
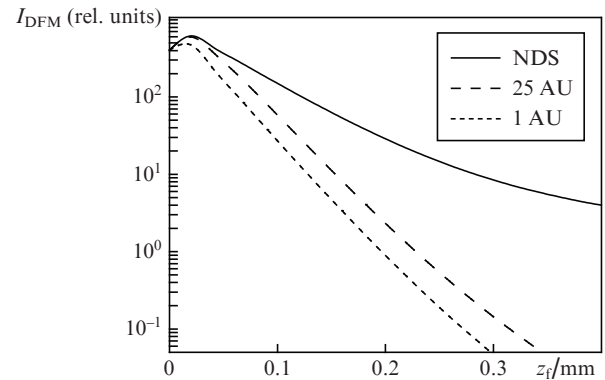

Figure 10. TPFM signal as a function of the focusing depth in a scattering medium, detected with the help of a NDS-receiver (solid line) and a DSCA-receiver (dashed lines) with the mentioned pinhole parameters at $\mu_{ex} = 10$ mm^{-1}, $\mu_{em} = 15$ mm^{-1}, $g = 0.9$, $n = 1.33$, $M_o = 20$, and NA = 1.

4. Conclusions

Analysis of the scattering effect on the image characteristics of optically thick biotissue samples, formed by two-photon fluorescence microscopy, requires a careful choice of the theoretical model. In this paper, by comparing the results of calculations with those of Monte Carlo simulations we have demonstrated the effectiveness of the modified small-angle diffusion approximation. This theoretical approach has been used to study the features of two-photon fluorescence excitation in a strongly scattering sample and to analyse the collection efficiency of the TPFM system. The results obtained make it pos-

sible to predict the nature of the fluorescence signal attenuation in TPFM setups equipped with various types of detectors.

References

1. Helmchen F., Denk W. *Nature Meth.*, **2**, 932 (2005).
2. Zipfel W.R., Williams R.M., Webb W.W. *Nature Biotechnol.*, **21**, 1368 (2003).
3. So P.T.C., Dong C.Y., Masters B.R., Berland K.M. *Ann. Rev. Biomed. Eng.*, **2**, 399 (2000).
4. Theer P., Denk W. *J. Opt. Soc. Am. A*, **23**, 3139 (2006).
5. Sergeeva E.A. *Kvantovaya Elektron.*, **40**, 411 (2010) [*Quantum Electron.*, **40**, 411 (2010)].
6. Larson D.R., Zipfel W.R., Williams R.M., Clark S.W., Bruchez M.P., Wise F.W., Webb W.W. *Science*, **300**, 1434 (2003).
7. Centonze V.E., White J.G. *Biophys. J.*, **75**, 2015 (1998).
8. Denk W., Piston D.W., Webb W.W., in *Handbook of Biological Confocal Microscopy*. Ed. by J.B. Pawley (New York: Springer Science+ Business Media, LLC, 2006) p. 535.
9. Nimmerjahn A., Theer P., Helmchen F., in *Ultrashort Laser Pulses in Biology and Medicine*. Ed. by M. Braun, P. Gilch, W. Zint (Berlin: Springer, 2008) p. 29.
10. Dunn A.K., Wallace V.P., Coleno M., Berns M.W., Tromberg B.J. *Appl. Opt.*, **39**, 1194 (2000).
11. Leray A., Odin C., Le Grand Y. *Opt. Commun.*, **281**, 6139 (2008).
12. Beaurepaire E., Mertz J. *Appl. Opt.*, **41**, 5376 (2002).
13. Xu C., Webb W.W. *J. Opt. Soc. Am.* B, **13**, 481 (1996).
14. Ishimaru A. *Wave Propagation and Scattering in Random Media* (New York: Acad. Press, 1978) Vol. 1.
15. Zege E.P., Ivanov A.P., Katsev I.L. *Image Transfer Through a Scattering Medium* (Heidelberg: Springer-Verlag, 1990).
16. Dolin L.S. *Izv. Akad. Nauk SSSR, Ser. Fiz. Atmos. Okean.*, **26**, 300 (1983).
17. Tuchin V.V. *Tissue Optics: Light Scattering Methods and Instruments for Medical Diagnosis* (Bellingham, WA: SPIE Press, 2007).
18. Sharma S.K., Banerjee S. *J. Opt. A: Pure Appl. Opt.*, **5**, 294 (2003).
19. Marchesini R., Bertoni A., Andreola S., Melloni E., Sichirollo A.E. *Appl. Opt.*, **28**, 2318 (1989).
20. Van der Zee P. *Measurement and Modelling of The Optical Properties of Hunan Tissue in The Near Infrared*. Ph.D. Thesis (University College London, 1992).
21. Gan X., Gu M. *Appl. Opt.*, **39**, 1575 (2000).
22. Leray A., Odin C., Huguet E., Amblard F., Le Grand Y. *Opt. Commun.*, **272**, 269 (2007).
23. Wang L., Jacques S.L., Zheng L. *Comp. Meth. Progr. Biomed.*, **47**, 131 (1995).
24. Milsom P.K. *Appl. Phys. B: Lasers and Optics*, **70**, 593 (2000).
25. Ying J., Liu F., Alfano R.R. *Appl. Opt.*, **38**, 224 (1999).
26. Dolin L.S. *Izv. Akad. Nauk SSSR, Ser. Fiz. Atmos. Okean.*, **18**, 840 (1982).
27. Pawley J.B., in *Handbook of Biological Confocal Microscopy*. Ed. by J.B. Pawley (New York: Springer Science+Business Media, LLC, 2006) p. 20.
28. Simpson C.R., Kohl M., Essenpreis M., Cope M. *Phys. Med. Biol.*, **43**, 2465 (1998).